Real-Time Compensation of Errors Caused by the Flux Density Non-uniformity for a Magnetically Suspended Sensitive Gyroscope

Xin Chaojun[1], Cai Yuanwen[1], Ren Yuan[1]*, Fan Yahong[2], and Su Yongzhi[1]

[1]Equipment Academy, Beijing, 101416, China
[2]Beijing Institute of Control Engineering, Beijing, 100108, China

Magnetically suspended sensitive gyroscopes (MSSGs) provide an interesting alternative for achieving precious attitude angular measurement. To effectively reduce the measurement error caused by the non-uniformity of the air-gap flux density in a MSSG, this paper proposes a novel compensation method based on measuring and modeling of the air-gap flux density. The angular velocity measurement principle and the structure of the MSSG are described, and then the characteristic of the air-gap flux density has been analyzed in detail. Next, to compensate the flux density distribution error and improve the measurement accuracy of the MSSG, a real-time compensation method based on the online measurement with hall probes is designed. The common issues caused by the non-uniformity of the air-gap flux density can be effectively resolved by the proposed method in high-precision magnetically suspended configurations. Comparative simulation results before and after compensation have verified the effectiveness and superiority of the proposed compensation method.

Keywords : Magnetically suspended sensitive gyroscope (MSSG), attitude angular measurement, non-uniformity, air-gap flux density, error compensation

1. Introduction

Due to a variety of priority as zero friction, high-speed operation, active vibration suppression, long life span and great potential of high control accuracy, active magnetic bearings (AMBs) have been successfully employed for many space missions as ideal actuator for the attitude control of the spacecraft [1-3]. Traditionally, AMBs are employed as control moment gyroscopes, moment wheels or reaction wheels in space missions [4, 5]. In recent years, researchers have begun to develop inertial sensors based on AMBs, named magnetically suspended sensitive gyroscope (MSSG) [6-8]. MSSG is used to measure attitude angle or angular velocities of the gyro-carrier. Compared to traditional mechanical gyroscopes, MSSG has a wide prospect of application in aerospace, aviation, navigation, homing, robots, and automobiles. The MSSG studies in this paper consists of a rotor and a stator, the rotor is levitated by the electromagnetic force produced from axial and radial magnetic bearings, and the Lorentz

force-type magnetic bearing (LFMB) is used as a torque [9]. By applying the Ampere's law and Euler dynamic equations, the attitude angular velocity of the gyro-carrier can be obtained by making use of the control currents in the LFMB.

The main advantage of LFMB is that the Lorentz force depends linearly on current. And the favorable linear properties and bidirectionality of the Lorentz force can simplify the analysis and design of the system when it is applied to stabilize the rotor position [10]. Whereas Maxwell-force based levitation requires ferromagnetic material, Lorentz-force-levitated devices can be built with nonferromagnetic stators, which eliminate parasitic forces and iron losses, reduce winding inductance, and improve the control accuracy [11].

Based on the assumption that the magnetic flux density in the air gap is homogenous, many researchers have developed different magnetically suspended apparatus with LFMB to suppress vibration [12, 13] and to achieve precise control [14-16]. Stephens et al. designed a new type of self-bearing motor, which used the Lorentz-type forces to produce both bearing force and motoring torque, and the tradeoff between motoring torque and bearing force is eliminated. Taken the distributing non-uniformity

*Corresponding author: Tel: +86-10-6636-4197
Fax: +86-10-6636-4198, e-mail: jingninan@126.com

into account, the air gap flux density has been approximated sinusoidal. However, the error between the sine wave approximation and the measured distribution is more than 20% [17], due to it contains odd orders of harmonic components [10]. Johan analyzed a compact conical Lorentz force self-bearing motor. The distributing non-uniformity of the flux density in the air gap has been considered, and it is assumed that the magnetic field can be approximated by a square wave [18]. Though some researches considered the distributing non-uniformity of the flux density in the air gap of a LFMB, few works have been done to study the change of Lorentz force caused by the distribution non-uniformity as the winding moves relative to the magnetic field. When the rotor tilts, the gap between the stator and rotor of LFMB changes nonlinearly, this will cause the magnetic force to be seriously nonlinear. The nonlinear change would lead to decreasing of the control accuracy directly. For the MSSG studies in this paper, the change would give rise to the measurement error of the angular velocity. Aiming to compensate the measurement error induced by the distributing non-uniformity of the flux density of a LFMB, thus improve the measurement accuracy of a MSSG, the distribution of the flux density has been analyzed, and the analytical expression of the angular velocity measurement error has been deduced firstly. Then, an universal method to compensate the non-uniformity error based on the flux density measuring in real-time has been proposed. At last, comparative simulations are constructed to testify the measurement performance with the proposed compensation method.

2. Angular Velocity Measurement Principle of a MSSG

2.1. Composition of a MSSG

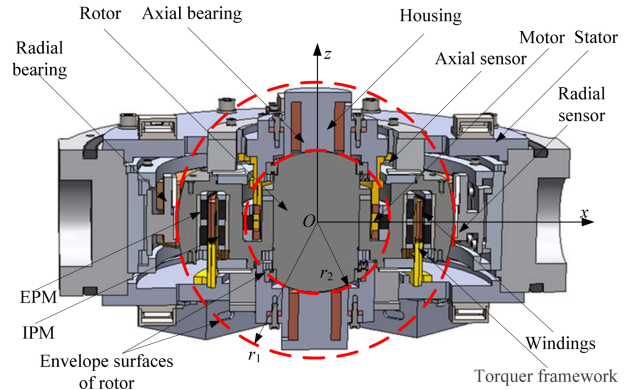Figure 1 shows the main configuration of the MSSG,

Fig. 1. (Color online) Configuration of the MSSG.

which consists of rotor, stator, high speed motor, torquer, a gyro house and displacement sensors *et al.* The rotor of the MSSG is a type of spherical in structure, and radiuses of rotor in axial and radial are r_1 and r_2, respectively. The rotor is levitating in the center of the stator cavity by magnetic pull produced by the interaction of the electromagnetic stator and the rotor. When the rotor is suspended in the center of the rotor housing, the bearing gap between the rotor and the inner surface of the stator magnetic poles is 0.35 mm. The rotation of the rotor is driven by a hollow cup permanent magnet brushless DC motor. When the magnetic pole envelope surfaces of stator and the rotor are ideal spherical surfaces, the magnetic forces over the entire surface of the rotor will pass through its geometric center and no torques acting on the rotor.

The torquer is a LFMB, which is used to control the tilting of the rotor. In the LFMB, the exterior permanent magnets (EPM) and the interior permanent magnets (IPM) are installed in the outer rim of the gyro rotor, and generate the approximately uniform air-gap magnetic flux circumferentially. Four windings are sticked on the framework of the LFMB stator symmetrically as shown in Fig.
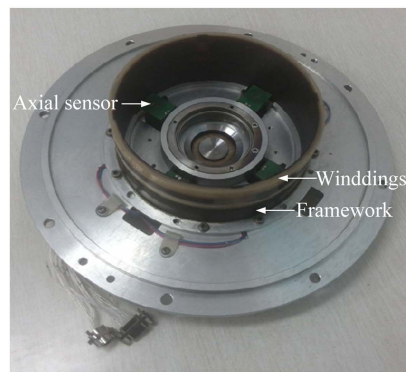
    (a) Rotor of the MSSG   (b) Stator of the LFMB

Fig. 2. (Color online) Structure of gyro rotor and stator of the LFMB.

2. If the windings are provided with control currents, the Lorentz force would be generated according Ampere rule. It is clear that the LFMB only provides force to control the tilting of rotor around x and y-axis by Lorentz force rather than to suspend it. The tilting angles are measured by the integrated axial/radial displacement sensors.

2.2. Principle of attitude angular measurement

When the gyro-carrier is static, the rotor is levitating in the center of the gyro house, spinning about z-axis at angular rate Ω. However, when the gyro-carrier fixed with the gyro house comes into an off-axis attitude angular rate $\boldsymbol{\omega}_{ib}$ related to the inertial space, the attitude of levitating rotor would remain the same dues to the gyroscopic inertia of the rotor. The displacement sensors would pick up the position changes of the rotor related to gyro house, and transmit the signals to control system. Control current will be applied to the windings according to the signals, compelling the rotor promptly rotate back to its equilibrium position at angular rate $\boldsymbol{\omega}_{ir}$ related to the inertial space.

The control bandwidth of the torquer and the measurement bandwidth of the sensors are much higher than the attitude change frequency of the gyro-carrier, so within the control bandwidth, the rotor would always track the attitude angular rate of the gyro-carrier in x- and y-axes, stabilizing the rotor at the predesigned equilibrium position.

Attitude angular rate of the gyro-carrier can be described as

$$\boldsymbol{\omega}_{ib} = \boldsymbol{\omega}_{ir} - \boldsymbol{\omega}_{rb} \tag{1}$$

where $\boldsymbol{\omega}_{rb}$ is the deflection angular velocity of rotor related to the gyro house. By using Euler dynamic equations, the equivalent moment acting on the rotor in x- and y-directions can be obtained,

$$\begin{cases} M_x = J_z \Omega \omega_{iby} + J_r \dot{\omega}_{ibx} \\ M_y = -J_z \Omega \omega_{ibx} + J_r \dot{\omega}_{iby} \end{cases} \tag{2}$$

where J_z is the polar moment of inertia of the rotor, and J_r is the equator moment of inertia of the rotor, ω_{ibx} and ω_{iby} is the attitude angular rate of gyro-carrier around x- and y-axes, respectively. M_x and M_y are torques acting on the rotor around x- and y-axes.

When the angular acceleration of the gyro-carrier is small, the above formula can be turned into gyroscopic effect precession equation since $J_z\Omega \gg J_r$, and the attitude angular rate of the gyro-carrier can be formulated as

$$\begin{cases} \omega_{iby} = \dfrac{M_x}{J_z \Omega} \\ \omega_{ibx} = -\dfrac{M_y}{J_z \Omega} \end{cases} \tag{3}$$

Ideally, the structure of the MSSG has determined the resultant moment acting on the levitating rotor generated from both the deflection control moments T_{dx}, T_{dy} produced by torquer and the gyroscopic moment caused by the deflection of the rotor $\boldsymbol{M}_e(0)$. Hence, the attitude angular rate of the gyro-carrier can be acquired indirectly by means of measuring the control moments from torquer and $\boldsymbol{M}_e(0)$.

The value of $\boldsymbol{M}_e(0)$ can be btained on the basis of gyroscope technology equations and angular displacement real-time measurement of the rotor, which can be expressed as

$$\boldsymbol{M}_e(0) = \begin{bmatrix} J_z\Omega\dot{\beta} + J_r\ddot{\alpha} \\ -J_z\Omega\dot{\alpha} + J_r\ddot{\beta} \\ 0 \end{bmatrix} \tag{4}$$

where α, β are the titled angles of the rotor about x- and y-axis respectively, and they can be acquired from

$$\begin{bmatrix} \alpha \\ \beta \end{bmatrix} = \begin{bmatrix} -\dfrac{d_{y+} - d_{y-}}{2l_s} \\ \dfrac{d_{x+} - d_{x-}}{2l_s} \end{bmatrix} \tag{5}$$

where d_{x+}, d_{x-} are the linear displacement in z-direction picked up by the sensors located at the positive and negative position in x-direction. l_s is the distance between sensor location and z-axes.

2.3. Deflection control moments

When a straight and stationary wire in magnetic field is excited by a current $\boldsymbol{i}$ perpendicularly towards the direction of flux intensity $\boldsymbol{B}$, it will experiences the Lorentz force, which can be written as

$$\boldsymbol{f} = \boldsymbol{i}L \times \boldsymbol{B} \tag{6}$$

where L is the length of wire, and the direction of current $\boldsymbol{i}$ is aligned with the direction of the wire.

Figure 3 shows the mechanism of LFMB in MSSG based on the above mentioned principle. The rotor of the LFMB consists of two ring-type permanents, which are fixed in the circumferential slot at the rim of the MSSG rotor. Four windings are sticked accurately symmetrically in the x- and y-axis on the stator of the LFMB, and the radius angles of the four windings are as follows,

$$\begin{aligned} &\text{Coil1}: (-\phi_0, \phi_0) \\ &\text{Coil2}: (90° - \phi_0, 90° + \phi_0) \\ &\text{Coil3}: (180° - \phi_0, 180° + \phi_0) \\ &\text{Coil4}: (270° - \phi_0, 270° + \phi_0) \end{aligned} \tag{7}$$
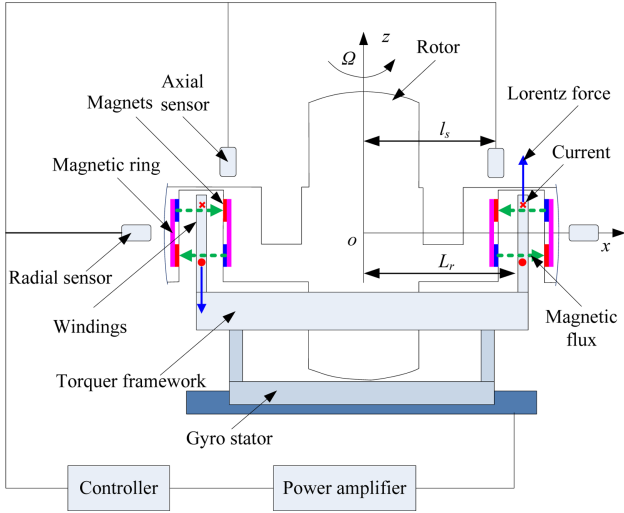
Fig. 3. (Color online) Mechanism of the LFMB.

where $\phi_0 = 35°$ is the half radius angle of each winding.

Ignoring the tiny angular displacement of the rotor, the torque generated from a wire element $Lr·d\phi$ can be expressed as

$$dT = r \times df = \begin{bmatrix} nL_r^2 i(t)B\sin\phi\,d\phi \\ -nL_r^2 i(t)B\cos\phi\,d\phi \\ 0 \end{bmatrix} \tag{8}$$

where r is the arm of Lorentz force, n is the turns of the Lorentz windings, L_r is the distance from the winding to rotor spinning axis, ϕ is the winding radius angle, $i(t)$ is the current in the windings measured in real-time, and B is the flux density of the circumferential magnetic field produced by the ring-type permanents.

If the Lorentz windings are provided with control current $i(t) = [i_{x+}(t)i_{y+}(t)-i_{x+}(t)-i_{y+}(t)]$, the integral LFMB torques according equation (8) can be expressed as

$$T = \begin{bmatrix} 8nL_r^2 i_{y+}(t)B\sin\phi_0 \\ -8nL_r^2 i_{x+}(t)B\sin\phi_0 \\ 0 \end{bmatrix} \tag{9}$$

where $i_{x+}(t)$, $i_{y+}(t)$ are the currents in the windings sticked in x- and y-directions respectively.

Substituting equations (9), (5) and (3) into (1) and (11), the attitude angular rate of gyro-carrier can be formulated as

$$\omega_b = \begin{bmatrix} \dfrac{8nL_r^2 i_{x+}(t)B\sin\phi_0}{J_z\Omega} - \dfrac{\dot{d}_{x+}-\dot{d}_{x-}}{2l_s} + J_r\dfrac{\ddot{d}_{y+}-\ddot{d}_{y-}}{2J_z\Omega l_s} \\ \dfrac{8nL_r^2 i_{y+}(t)B\sin\phi_0}{J_z\Omega} - \dfrac{\dot{d}_{y+}-\dot{d}_{y-}}{2l_s} - J_r\dfrac{\ddot{d}_{x+}-\ddot{d}_{x-}}{2J_z\Omega l_s} \end{bmatrix} \tag{10}$$

It is obvious that the attitude angular rate of gyro-carrier can be obtained by means of measuring the control current in Lorentz windings and the linear displacement of gyro rotor in real-time, realizing the attitude angular rate measuring in two degrees of freedom with single MSSG.

3. Analysis of Errors Caused by Flux Density Distribution Non-uniform

3.1. Distribution analysis of flux density in the air gap

If the LFMB consists of a structure with constant physical dimensions and constant air gap flux density and hence the produced torques are proportional to the winding currents, in other words the currents directly give the attitude angular rates of the gyro-carrier in the responding axis. In general, the B value in equation (10) is obtained by means of static calibration. However, the distribution of the magnetic field distributing in the air gap is non-uniform as a matter of fact.

To verify the actual distribution of the magnetic field in
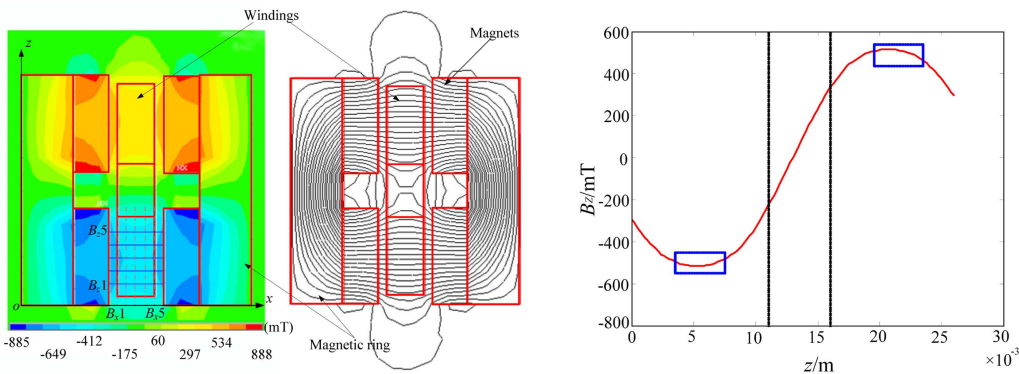
(a) Flux density in the air gap on a cross-section   (b) Distribution curve of the flux density axially

Fig. 4. (Color online) Distribution of the flux density in the air gap.

(a) Distribution of the flux density radially　　(b) Distribution of the flux density axially
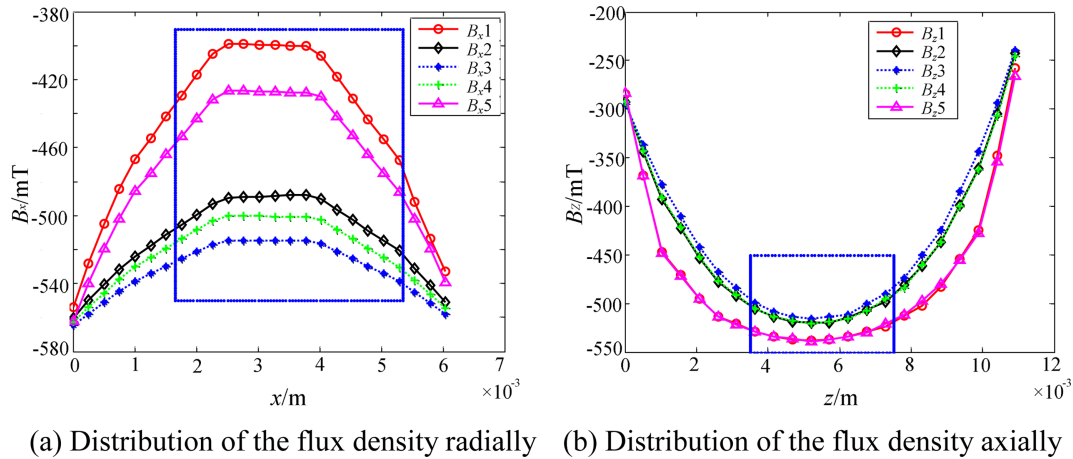
Fig. 5. (Color online) Flux density at different locations of the air gap.

the air gap, the finite element method and experiment are employed. Figure 4(a) show the isovalues and isolines of the flux density in the air gap on a cross-section. Figure 4(b) gives the distribution curve of the flux density in axial on the centerline of the air gap. As it can be seen from Fig. 4(a), the magnetic field between the exterior and interior PM rings is non-uniform. On one hand, the flux density distribution between upper PM rings is similar to the lower ones but in the opposite direction. On the other hand, the flux density between the outer and inner PM rings appears high in the center and low in both sides in axial, and low in the center and high in both sides in radial. According to Fig. 4(b), we can discover that the distribution curve of the flux density in axial approximates a sine curve, and the magnetic field on the active part of the windings is surely non-uniform.

In order to analyze the magnetic field in air gap quantitatively, the flux density distributions at different locations as marked in Fig. 4(a) are analyzed. Figure 5 indicates the flux density distributions in axial and radial respectively. The dashed boxes indicate the active parts of the windings both in Fig. 4 and Fig. 5.

From Fig. 5(a), we can summarize that the flux density distribution is nonlinear radially in the lower PM rings. The maximum appear at both sides of each location due to nearing the PM, and in the center sections, the flux densities hold constant values. At the locations $Bx1$ and $Bx5$ which near the edges of the air gap in axial, the flux density rates of change reach the maximum. And the active parts of the winding obviously lie in the section which contains the flux density non-uniformity. From Fig. 5(b), we can also see that the flux density distribution in axial is nonlinear. The flux density reaches the maximum in the center and decrease gradually in axial.

Except the above mentioned nonlinearity of the flux

density caused by the static distribution of the magnetic field in LFMB, the deflection of the rotor, the interaction of the electromagnetic field and the PM magnetic field may also produce changes of flux density at locations of the windings. According to equation (6), the changes of the flux density at locations of the windings are bound to lead changes of the Lorentz force, therefore result in errors in the measured attitude angular rate of the gyro-carrier. When the rotor titled, the relative displacement would come into being between the windings and the PM rings on rotor. The bounds of the rotor titling are $\pm 0.3°$. Without regarding the vibration of the rotor, the motion ranges of a single Lorentz winding in radial-direction is -0.0111 mm $< x < 0.0098$ mm, and in axial-direction is -0.2562 mm $< z < 0.2561$ mm. It means that when the rotor deflects the displacement of winding related to rotor is much larger in axial-direction than that in radial-direction, and the flux density non-uniformity in axial-direction has a more important influence to the measurement accuracy. Considering the above reason, the non-uniformity in axial-direction is mainly taken into account in this paper, and we can assume the flux density of LFMB is approximately correlated with the axial position, written as $B(z)$.

3.2. Analysis of the measurement errors

Selecting the circumference angular element $d\phi$ on the Lorentz winding, and axial element dz, the Lorentz force generated from the winding element in axial by a exciting current i can be described as

$$df = \left\{ \int_{z_d}^{z_u} \frac{n}{Z_0} \left[i \times \boldsymbol{B}(z) \right] dz \right\} L_r d\phi \qquad (11)$$

where $Z_0 = z_u - z_d$ denote the height of the windings in axial, z_d and z_u are the distances from the lower and upper

edges to the *xoy*-plane, respectively. The direction vector of the current can be expressed as $[-\sin\phi \ \cos\phi \ 0]^T$ and that of the flux density can be expressed as $[\cos\phi \ \sin\phi \ 0]^T$ when the rotor is spinning at its equilibrium position.

However, when the rotor tilted α about *x*-axes and β about *y*-axes respectively, the PM rings will also tilted the same angles with rotor, which would result in change of the angle between the wire element and its corresponding flux density. Thus the direction vector of the flux density turns as

$$
\begin{bmatrix}
\cos\beta\cos\phi + \sin\alpha\sin\beta\sin\phi \\
\cos\alpha\sin\phi \\
-\sin\beta\cos\phi + \sin\alpha\cos\beta\sin\phi
\end{bmatrix} =
$$
$$
\begin{bmatrix}
\cos\beta & 0 & \sin\beta \\
0 & 1 & 0 \\
-\sin\beta & 0 & \cos\beta
\end{bmatrix}
\begin{bmatrix}
1 & 0 & 0 \\
0 & \cos\alpha & -\sin\alpha \\
0 & \sin\alpha & \cos\alpha
\end{bmatrix}
\begin{bmatrix}
\cos\phi \\
\sin\phi \\
0
\end{bmatrix}
\tag{12}
$$

According Equation (11) and (8), the Lorentz force and torque can be written as

$$
df = \left\{
\begin{array}{l}
\int_{z_d}^{z_u} \dfrac{n}{Z_0} i(t) B_1(z) \\
\begin{bmatrix}
[-\sin\beta\cos\phi + \sin\alpha\cos\beta\sin\phi]\cos\phi \\
[-\sin\beta\cos\phi + \sin\alpha\cos\beta\sin\phi]\sin\phi \\
-\cos\alpha\sin^2\phi - \cos\phi[\cos\beta\cos\phi + \sin\alpha\sin\beta\sin\phi]
\end{bmatrix} dz
\end{array}
\right\} L_r \, d\phi
\tag{13}
$$

$$
d\boldsymbol{T} = \left\{
\int_{z_d}^{z_u} \dfrac{n}{Z_0} i(t) B_1(z)
\begin{bmatrix}
L_r(-\cos\alpha\sin^3\phi - \cos\beta\sin\phi\cos^2\phi \\
-\sin\alpha\sin\beta\sin^2\phi\cos\phi) \\
-z(-\sin\beta\sin\phi\cos\phi + \sin\alpha\cos\beta\sin^2\phi) \\
L_r(\cos\alpha\sin^2\phi\cos\phi + \cos\beta\cos^3\phi \\
+\sin\alpha\sin\beta\sin\phi\cos^2\phi) \\
+z(-\sin\beta\cos^2\phi + \sin\alpha\cos\beta\sin\phi\cos\phi) \\
0
\end{bmatrix}
dz
\right\} L_r \, d\phi
\tag{14}
$$

where $i(t)$ denotes the measured control current, and $B_1(z)$ denotes the magnitude of flux density after rotor tilted.

Injecting the opposite windings with opposite current, and integrating the torque in the winding circumferences angular, the resultant torque can be formulated as

$$
\boldsymbol{T}_1 + \boldsymbol{T}_3 = \int_{z_{pd1}}^{z_{pu1}} f[i_1(t)] B_{p1}(z) dz + \int_{z_{nd1}}^{z_{nu1}} f[i_1(t)] B_{n1}(z) dz
$$
$$
+ \int_{z_{pd3}}^{z_{pu3}} f[i_1(t)] B_{p3}(z) dz + \int_{z_{nd3}}^{z_{nu3}} f[i_1(t)] B_{n3}(z) dz
$$
$$
\boldsymbol{T}_2 + \boldsymbol{T}_4 = \int_{z_{pd2}}^{z_{pu2}} f[i_2(t)] B_{p2}(z) dz + \int_{z_{nd2}}^{z_{nu2}} f[i_2(t)] B_{n2}(z) dz
\tag{15}
$$
$$
+ \int_{z_{pd4}}^{z_{pu4}} f[i_2(t)] B_{p4}(z) dz + \int_{z_{nd4}}^{z_{nu4}} f[i_2(t)] B_{n4}(z) dz
$$
$$
\boldsymbol{T} = \boldsymbol{T}_1 + \boldsymbol{T}_3 + \boldsymbol{T}_2 + \boldsymbol{T}_4
$$

where z_{pui} ($i = 1, 2, 3, 4$) is the distances from the upper edge of the *i*th winding upper part to the *xoy*-plane, and z_{pdi} ($i = 1, 2, 3, 4$) is the distances from the lower edge of the *i*th winding upper part to the *xoy*-plane. z_{nui} ($i = 1, 2, 3, 4$) is the distances from the lower edge of the *i*th winding lower part to the *xoy*-plane, and z_{ndi} ($i = 1, 2, 3, 4$) is the distances from the lower upper edge of the *i*th winding lower part to the *xoy*-plane. B_{pi} ($i = 1, 2, 3, 4$) is the flux density of LFMB at the location of the *i*th winding upper part, and B_{ni} ($i = 1, 2, 3, 4$) is the flux density of LFMB at the location of the *i*th winding lower part. $f[i_1(t)], f[i_2(t)]$ can be written as

$$
f[i_1(t)] = \frac{n}{Z_0} L_r^2 i_1(t)
\begin{bmatrix}
\left(-\dfrac{4}{3}\sin\alpha\sin\beta\sin^3\phi_0\right) \\
\left(\dfrac{4}{3}\cos\alpha\sin^3\phi_0 + 4\cos\beta\sin\phi_0 - \dfrac{4}{3}\cos\beta\sin^3\phi_0\right) \\
0
\end{bmatrix}
$$

$$
f[i_2(t)] = \frac{n}{Z_0} L_r^2 i_2(t)
\begin{bmatrix}
\left(-4\cos\alpha\sin\phi_0 + \dfrac{4}{3}\cos\alpha\sin^3\phi_0 - \dfrac{4}{3}\cos\beta\sin^3\phi_0\right) \\
\left(\dfrac{4}{3}\sin\alpha\sin\beta\sin^3\phi_0\right) \\
0
\end{bmatrix}
\tag{16}
$$

Substituting equation (15) into (10), we can obtain the attitude angular rate of the gyro-carrier taking the non-uniformity of air-gap flux density into consideration.

Obviously, if we adopt the value of flux density from static calibration to calculate the attitude angular rate in equation (10) without considering the non-uniformity of air-gap flux density, the measurement error comes into being. The relative measurement error can be written as

$$
\delta\omega_{ib} = \tilde{\omega}_{ib}(B) - \hat{\omega}_{ib}(B(z))
\tag{17}
$$

where $\tilde{\omega}_{ib}(B)$ is the measured angular velocity and $\hat{\omega}_{ib}(B(z))$ is the true value of input angular velocity.

4. Compensation Based on the Flux Density Measuring in Real-time

The non-uniformity of air-gap flux density, the relative displacement of windings and magnetic field, and the interaction of the electromagnetic field and the PM magnetic field would lead changes to magnitude and direction of flux density at the winding locations simultaneously. In order to deduce the affection of changing flux density at the winding locations, an on-line error compensation method is proposed in this section based on flux density measuring in real-time.
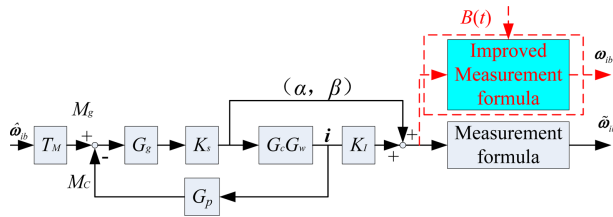
By means of installing high accuracy hall probe at the

Fig. 6. (Color online) Schematic diagram of the error correct method.

center of the active part of LFMB windings in axial, the flux density at the axial locations of windings can be measured in real-time. Thus the inaccuracy of the flux density at the axial locations of windings would be eliminated at the same time. Substituting the value of flux density measured in real-time into Equation (10), the high accuracy measurement of attitude angular rate can be realized.

Figure 6 reveals the schematic diagram of the error correcting method. The part drawing in real lines is the original method. T_m is the transfer function of torque converter, which transform the angular motion $\hat{\omega}_{ib}$ of the gyro-carrier into gyro coupling torques M_g acting on the rotor. M_C is the control torques produced by the LFMB according to the controller signals, whose transfer function is G_p. G_g is the transfer function of the rotor, and K_s is the model of displacement sensors. G_cG_w is the transfer function of gyro controller and amplifier, whose output could be picked by the current sensors and be applied with the angular displacements in Equation (11) to calculate the measured angular velocity $\tilde{\omega}_{ib}$, and K_I is the model of current sensors.

However, in original method the value of flux density needed in Equation (11) is usually obtained from static calibration. Because the value of flux density from static calibration neglected the non-uniformity and motion of the PM magnetic field, the calculated attitude angular rate undoubtedly contains measuring errors.

The dashed box in Fig. 6 indicates the improved method to correct the measuring error. And $B(t)$ denotes the real-time measured value of flux density at the axial locations of windings. By applying $B(t)$ as the key resolving parameter, the high accuracy measured value of attitude angular rate can be acquired base on improved measurement equation.

Figure 7 is the structure picture of the error correcting system. The installing locations of the eight hall probes on the support framework are labeled in Fig. 7(a). The system includes eight teslameters with a micro high accuracy hall probe. The measurement precision of the hall probe is 0.05%, and the length of which is only 6 mm, as is shown in Fig. 7(b). The eight hall probes are fixed symmetrically in circumferential. Each probe is installed at the middle of the gap between the active parts of two continual windings. The measurement centers are aligned with the centers of active part of the windings axially and radially.

When the rotor is spinning at its equilibrium position, the flux density in the air gap was measured by the hall probes, the measurement equipment and experiment results are shown in Fig. 8. From Fig. 8, we can conclude that the distribution of the flux density are approximately uniform in circumferential but reliably non-uniform in axial at the location of windings. The actual magnetic field distribution in axial direction of the LFMB is shown in Fig. 9. Due to the height of the windings in axial, the relative motion between rotor and the stator of the LFMB is limited in a certain range when the gyro-carrier rotated. The motion ranges of the upper and lower fringes of a single Lorentz winding in z-direction are indicated in Fig.
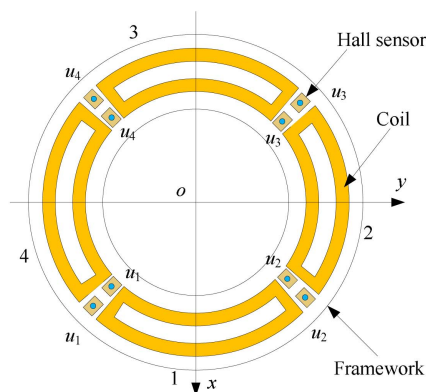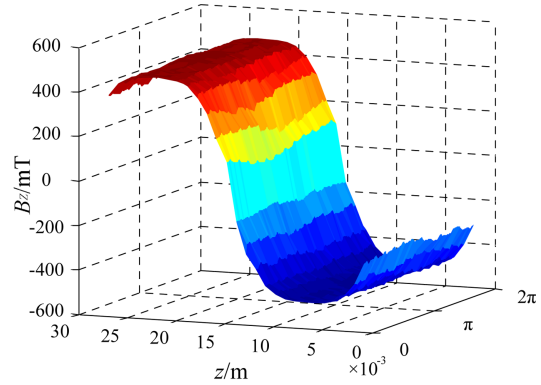

(a) Positions of the Hall probes

(b) Structure of the Hall probes

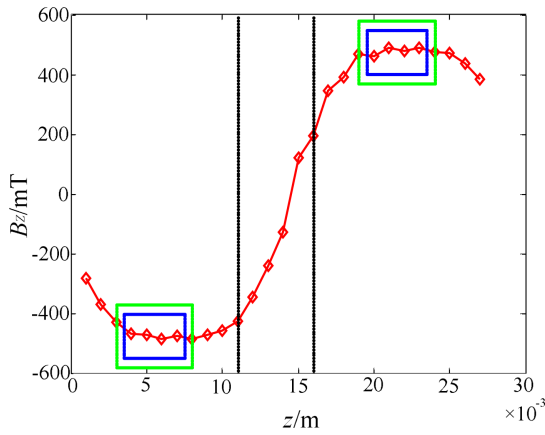**Fig. 7.** (Color online) Structure of the error correcting system.
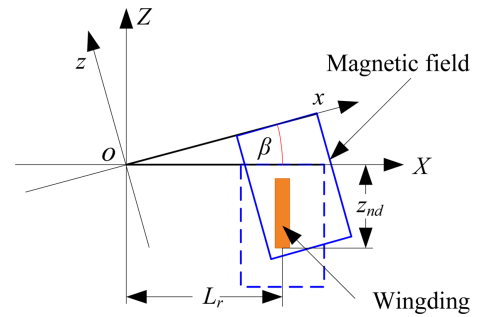
(a) Measurement equipment

(b) Experiment results of the flux desity

Fig. 8. (Color online) Measurement equipment and experiment results.


Fig. 9. (Color online) Actual distribution of the flux density axially.

Fig. 10. (Color online) Motion range of the lower winding.

9 in dash (green) lines while the wingding fringes are indicated in dash (blue) lines. When the rotor is spinning at its equilibrium position, the central site location of the wingding lower fringe can be written as $[L_r\ 0\ z_{nd}]$ in rotor

coordinate system $o\text{-}xyz$. However, when the rotor deflects β around y-axis, because of the winding stays still, the central site location of the wingding lower fringe becomes to $[L_r\cos\beta + z_{nd}\sin\beta\ 0\ -L_r\sin\beta + z_{nd}\cos\beta]$ in rotor coordinate system $o\text{-}xyz$, as is shown in Fig. 10. Considering the bounds of the rotor titling are $\pm 0.3°$ and the actual thickness of the windings, the motion ranges of the lower and upper fringes can be calculated as 3.3-7.7 mm and 18.3-
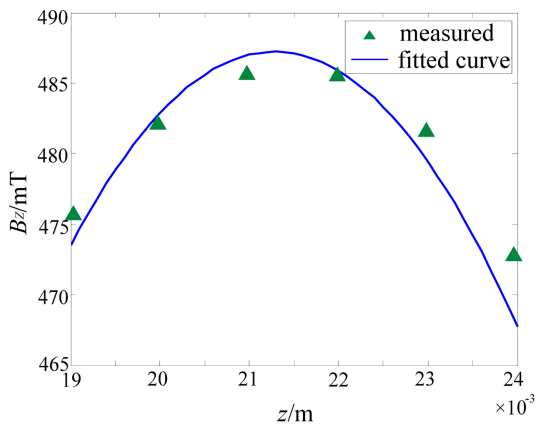
(a) Fitted curve from the upper hall probes
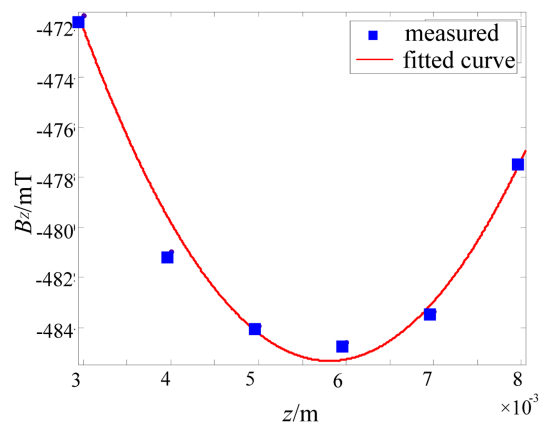
(b) Fitted curve from the lower hall probes

Fig. 11. (Color online) Fitted curves of flux density in the hall probes motion ranges.

22.7 mm respectively.

According to the measurement results, the fitted equations of flux density in the motion ranges of the upper and lower hall probes can be acquired. After fitting the data with least square method, the relationship between the flux density and the axial position can be expressed as

$$B(z)_{up} = -2.638z^2 + 17.32z + 458.8 \quad (18)$$

$$B(z)_{down} = 1.618z^2 - 12.82z - 460.9 \quad (19)$$

And the fitted curves are shown in Fig. 11.

On the basis of the real-time measurement values of the hall probes fixed on both sides of the winding 1, $B(z,t)_{u1}$, $B(z,t)_{u2}$, $B(z,t)_{d1}$, $B(z,t)_{d2}$, the axial position of the hall probes can be acquired, on the upper side, they can be written as equation (20), and on the lower side, they can be written as equation (21).

$$z_{u1} = -\frac{17.32 - \sqrt{17.32^2 + 4 \times 2.638 \times [458.8 + B(z,t)_{u1}]}}{2 \times 2.638}$$

$$z_{u2} = -\frac{17.32 - \sqrt{17.32^2 + 4 \times 2.638 \times [458.8 + B(z,t)_{u2}]}}{2 \times 2.638} \quad (20)$$

$$z_{d1} = \frac{12.82 - \sqrt{12.82^2 + 4 \times 1.618 \times [460.9 + B(z,t)_{d1}]}}{2 \times 1.618}$$

$$z_{d2} = \frac{12.82 - \sqrt{12.82^2 + 4 \times 1.618 \times [460.9 + B(z,t)_{d2}]}}{2 \times 1.618} \quad (21)$$

Take the average value of the two hall probes positions on both sides of the winding active parts as the centers of the winding, the distances from the upper and lower edges to the *xoy*-plane of each active part can be formulated as

$$z_{u1} = \frac{z_{up1} + z_{up2}}{2} - \frac{Z_0}{2}$$

$$z_{u2} = \frac{z_{up1} + z_{up2}}{2} + \frac{Z_0}{2} \quad (22)$$

$$z_{d1} = \frac{z_{down1} + z_{down2}}{2} - \frac{Z_0}{2}$$

$$z_{d2} = \frac{z_{down1} + z_{down2}}{2} + \frac{Z_0}{2} \quad (23)$$

Substituting equations (22), (23) into the expression of the Lorentz torque, the real-time Lorentz torque produced by single Lorentz winding 1 can be written as

$$T_1(t) = \int_{z_{u1}}^{z_{u2}} f[i_1(t)]B(z,t)_{u1} dz + \int_{z_{d1}}^{z_{d2}} f[i_1(t)]B(z,t)_{d1} dz \quad (24)$$

Substitute the actual measurement results in real-time of the flux density into equation (24), the accurate angular velocity of the gyro-carrier can be achieved by using

equation (10), and the errors induced by the non-uniformity of air-gap flux density in LFMB can be corrected.

5. Simulation Results

In this section, we conduct the simulations of the proposed method to verify the satisfactory correction effect under the rated rotor speed 10000 r/min. And the simulations are put up on the assumption that there are no other disturbing torques come into being. The system parameters of the MSSG are shown in Table 1.
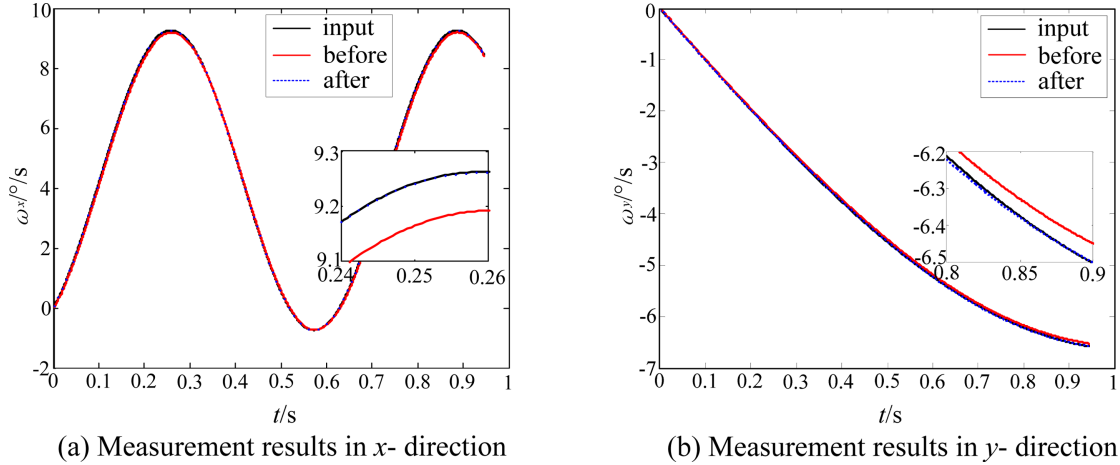
When there are angular velocity inputs in *x*- and *y*-direction, respectively, the measurement results according to Equation (10) would inevitably contain errors produced by the non-uniformity of the air-gap flux density as shown in Fig. 8(b). However, when it comes to the proposed method, the measurement accuracy of angular velocity for a MSSG can be improved greatly using analytical way to compensate the above mentioned errors. Figure 12 shows the comparative simulation results of the measured angular velocity before and after compensating. In the figure, the real (black) denotes the actual angular velocity input, and the real red and dotted blue lines delegate the measured results before and after compensating respectively.

According to Fig. 12, both the measured results by two different methods show deflections to the actual angular velocity input, and the deflections increase as the actual angular velocity input becomes higher. However, the measured results acquired by the method proposed in this article are clearly closer to the input value.
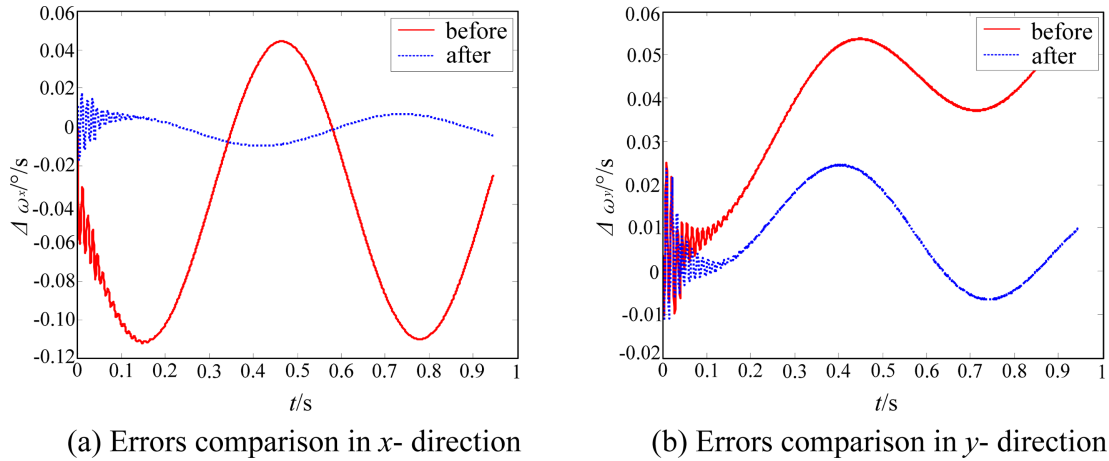
Figure 13 reveals the effectiveness of the proposed compensation method, the measurement errors in *x*- and *y*-direction are compared before and after compensation. In the figures, the real (red) line delegates the measurement error before compensation, and the dotted (blue) line represents the measurement error after compensation. According to Fig. 13, we can find that the measurement errors in *x*- and *y*- direction have been greatly reduced. Before compensation, the plus and minus peak values of measurement errors are 0.048°/s and −0.115°/s respectively

Table 1. System parameters of the MSSG.

parameter (unit)	numerical value	parameter (unit)	numerical value
m (kg)	4.7	J_r (kg·m^2)	0.0034
Ω (r/min)	10000	J_z (kg·m^2)	0.0052
n	50	r_1 (m)	0.07865
ϕ_0 (°)	35	r_2 (m)	0.041
L_r (m)	0.04892	Z_0 (m)	0.004
B (T)	0.484	l_s (m)	0.087

(a) Measurement results in *x*- direction   (b) Measurement results in *y*- direction

Fig. 12. (Color online) Angular velocity measurement results before and after compensation.

(a) Errors comparison in *x*- direction   (b) Errors comparison in *y*- direction

Fig. 13. (Color online) Measurement errors before and after compensation.

in *x*- direction, and the peak value of measurement error in *y*- direction is 0.058°/s. As for the proposed method, the plus and minus peak values have been decreased to 0.007°/s and −0.01°/s, the measurement accuracy has improved for approximately 85% in *x*- direction. Meanwhile, the peak value of measurement error in *y*- direction has been decreased to 0.025°/s, and the measurement accuracy has improved for approximately 55%. The residual errors are resulted in the approximation of the winding positions and the curve fitting errors, as position of the winding was approximated by the average value of the two hall probes' on both sides of the winding but the practical positions.

The results confirm the point that the measurement errors produced by the non-uniformity of air-gap flux density have been greatly compensated by the proposed method in this paper. The measurement errors in both the same axis and orthogonal axis have been greatly reduced. And the simulation result is in accordance with the

analysis in Section 3 and Section 4.

6. Conclusion

Theoretical analysis and experimental measurement show that the air-gap flux density of the MSSG is non-uniform axially and radially. According to the angular velocity measurement principle of the MSSG, the non-uniformity of the air-gap flux density would inevitably induce the angular velocity measurement errors. To compensate the measurement errors caused by non-uniformity of the air-gap flux density in the newly developed MSSG, a novel online compensation method based on flux density measuring in real time is proposed in this paper. By analyzing the distribution characteristics of the air-gap flux density and founding the analytical model of the measurement error, the principle of the compensation system is presented in detail. Simultaneity, models of torque output in real time and key flux density distribu-

tion in axial are established by experiment. Simulations results demonstrate that with the proposed compensation method the measurement error can be reduced approximately 80% and 55% in *x*- and *y*- direction, respectively, therefore increasing the measurement accuracy of angular velocity for a MSSG. To sum up, by means of installing the hall probes in the MSSG, the presented method can effectively compensate the measurement error caused by non-uniformity of the air-gap flux density, realizing its high-precision attitude measurement. The same compensation method can be extended to other high-precision magnetically suspended configurations for further study.

References

[1] B. C. Han, S. Q. Zheng, Z. Wang, and Y. Le, IEEE Trans. Ind. Electron. **62**, 7424 (2015).

[2] P. L. Cui, J. Cui, Q. Yang, and S. Q. Zheng, Math. Probl. Eng. **2015**, 1 (2015).

[3] P. L. Cui, S. Li, and C. Peng, IEEE/ASME Trans. Mechatron. **21**, 618 (2016).

[4] Y. Ren and J. C. Fang, IEEE Trans. Ind. Electron. **61**, 1539 (2014).

[5] J. C. Fang, Y. Ren, and Y. H. Fan, IEEE Trans. Ind. Elec-tron. **61**, 2003 (2014).

[6] Y. Maruyama, T. Mizuno, M. Takasaki, Y. Ishino, and H. Kameno, J. Mechatronics **19**, 1261 (2009).

[7] Y. Maruyama, T. Mizuno, M. Takasaki, Y. Ishino, H. Kameno, and A. Kubo, J. Sys. Design Dyna. **3**, 954 (2009).

[8] T. Akiyama, T. Mizuno, M. Takasaki, Y. Ishino, and K. Obara, Mechatronics **24**, 1059 (2014).

[9] C. J. Xin, Y. W. Cai, Y. Ren, and Y. H. Fan, J. Magn. **21**, 356 (2016).

[10] S. Park and C. Lee, IEEE/ASME Trans. Mechatron. **10**, 618 (2006).

[11] R. G. Thomas and F. L. Alan, IEEE Trans. Control Syst. Technol. **29**, 74 (2009).

[12] T. M. Lim and D. S. Zhang, Mechatronics **18**, 35 (2008).

[13] T. M. Lim and D. S. Zhang, Artif. Organs **30**, 347 (2006).

[14] J. Q. Tang, B. Xiang, and C. E. Wang, ISA Trans. **58**, 509 (2015).

[15] C. E. Wang and J. Q. Tang, Math. Probl. Eng. **2013**, 147 (2013).

[16] B. Xiang and J. Q. Tang, Mechatronics **28**, 46 (2015).

[17] L. S. Stephens and D. G. Kim, IEEE Trans. Magn. **38**, 1764 (2002).

[18] A. Johan, O. Jim, and H. Magnus, IEEE Trans. Magn. **50**, 1 (2014).